Journal of Materials Chemistry C

Accepted Manuscript

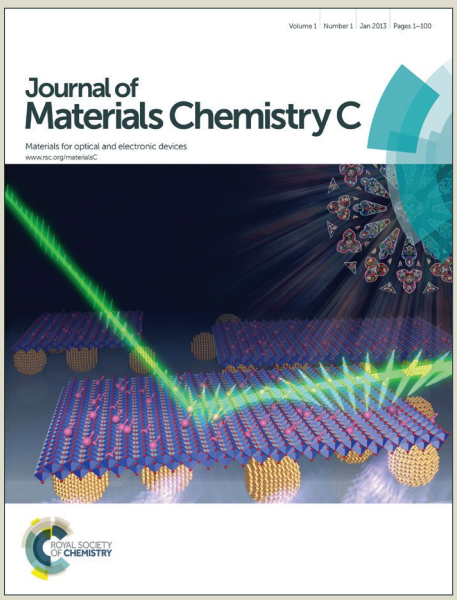

ROYAL SOCIETY OF CHEMISTRY

www.rsc.org/materialsC

Journal of Material Chemistry C

ARTICLE

Effect of solvent, pH and metal ions on the self-assembly process and optical properties of an A-π-D-π-A type triphenylamine carboxylic acid derivative

Received 00th January 20xx,
Accepted 00th January 20xx

DOI: 10.1039/x0xx00000x

www.rsc.org/

Lin Kong,*[a,c] Yun Liu,[a] Hui Wang,[a] Xiao-He Tian,[b] Qi-Yu Chen,[a] Yu-peng Tian,[a] Sheng-li Li,[a] Zhao-ming Xue[a] and Jia-xiang Yang*[a]

A 'Λ' structural A-π-D-π-A type triphenylamine derivative (2E,2'E)-3,3'-(4,4'-(phenylazanediyl)bis(4,1-phenylene))diacrylic acid (abbreviated as **L**) with intramolecular charge transfer (ICT) character has been designed, synthesized and characterized. The morphology and linear optical properties of **L** nanostructures can be tuned by changing the solvent and/or the acidity of the solution. The possible growth mechanism is discussed through the single crystal structure and the corresponding molecular stacking style of **L** molecules. Further, the strong coordination effect between carboxylic acid group of **L** and metal ions is discussed, which also brings about changeable morphology, linear optical properties and enhanced nonlinear optical properties, two photon absorbance (TPA) included, which make them suitable for application in two-photon biological imaging, such as in HepG2 cells.

1 Introduction

In the past few decades, self-assembly of functional organic molecules has attracted increasing attention owing to their unique electronic and/or photonic properties [1], which can be used as potential candidates of active components in organic light emitting diodes (OLEDs), organic field-effect transistors (OFETs), and solar cells, etc [2]. The electric and/or photophysical properties of these organic nanomaterials can be changed due to the morphology including size [3], shape [4] and crystallinity [5], which are considered to be associated with changes in the molecular packing modes, external environments and growth time. The weak noncovalent intermolecular interactions such as hydrogen bonding, van der Waals froces, π-π stacking and electrostatic interactions, etc [6] are very important that can tune the self-assembly process, which can be realized through rational and simple approach to change the external environments. Up to now, the self-assembly process to get organic nanomaterials is still highly desirable for the advancement of organic nanoscience and nanotechnology [7]. Thus, the choice of materials based on the predication of structure-property relationship shows important significance in this field.

Amongst the functional organic molecules, intramolecular charge-transfer (ICT) compound is an important class to be used to regulate structure easily in nanometer scale under different environment through self-assembly process. An ICT molecule possesses an electron-donating (D) group and an electron-accepting (A) group, which are connected through a π-conjugated bridge. The charge can be partly transferred from D group to A group, which renders the molecule somewhat strong D-A dipole-dipole interactions. Thus, self-assembly of an ICT compound in nano- or micro-meter size can be controlled effectively along the direction of the dipole-dipole interactions [8]. In addition, other weak intermolecular interactions as described previously also play important roles in constructing the organic nano/microstructures. So, the preparation parameters such as solvent, concentration, pH value of the solution, temperature, growth time, the existence of metal ions, and so on, can influence the self-assembly process of an ICT compound [9], which can further bring about changeable and/or optimized morphology and the corresponding optical properties.

In selecting the ICT molecule with wealth of weak intermolecular interactions, the carboxylic acid derivatives are good candidates. As is well-known that the carboxylic acid derivatives display interesting multitudinous supramolecular interactions [10], among which hydrogen bonding interaction is the main force. Thus the self-assembly process of an ICT type carboxylic acid derivative can be influenced by the environmental factor such as solvent with different polarity, pH value, etc [11]. Moreover, the carboxylic derivative can act directly with metal ions in constructing coordination polymer particles (CPPs) [12] based on the coordination-directed assembly of metal ions and organic carboxylic acid bridging ligands, due to deprotonation effect of the carboxylic acid unit [13]. The alkaline earth metal ions, transition metal ions and rare earth metal ions are often used to synthesize this type of

[a] Department of Chemistry, Key Laboratory of Inorganic Materials Chemistry of Anhui Province, Anhui University, 111th Jiu-Long Road, Hefei, P.R. China.
[b] College of life science, Anhui University, 111th Jiu-Long Road, Hefei, P.R. China.
[c] State Key Laboratory of Rare Earth Resources Utilization, Changchun Institute of Applied Chemistry, Chinese Academy of Sciences, 5625 Renmin Street, Changchun 130022, Jilin, PR China.
*Corresponding author: konglin_2009@126.com; jxyang@ahu.edu.cn
Electronic Supplementary Information (ESI) available: Selected bond lengths [Å] and angles [°] for **L**; The powder X-ray diffraction and the infrared spectra of **L** and coordination polymers.

CPPs, not only because of their fascinating architectures but also their optical and electronic properties [14]. The properties of these CPPs depend not only on the size, shape and composition but also to a large extent on the molecular stacking style within a material and the crystallinity of them [5, 15]. These factors can be easily regulated through changing external environment. The changeable properties make them attractive for many scientific and industrial areas such as electronics [16], photonics [17], sensors [18], medicine [19], biotechnology [13, 20] and environmental technology [21].

Considering all the above aspects, in this study, a carboxylic derivative, (2E,2'E)-3,3'-(4,4'-(phenylazanediyl)bis(4,1-phenylene))-diacrylic acid (abbreviated as **L**) [22], has been designed and synthesized, among which the triphenylamine unit is employed as electron-donor group and carboxylic acid unit is used as electron acceptor group, the two parts are connected through the double bond to construct A-π-D-π-A type molecule which possesses ICT effect as the main feature. **L** is a typical ICT compound which has attracted many interests. In 2007 and 2008, Murphy reported the synthesis of this type of compounds [23]. In 2012, Singh and his co-workers used it as the intermediate product for further synthesis [24]. The main purpose of this study is to research the influence of external environment on the morphology and the corresponding optical properties of **L**. Thus, the influence of solvent with different polarity, pH value of the solution and the existence of metal ions on the self-assembly process of **L** is studied in detail. The possible mechanism of the changeable morphology is discussed through the single crystal structure and the molecular stacking style. The different morphologies obtained under these features bring about changeable linear and nonlinear optical properties. Further, the coordination effect of **L** and three metal ions (Ba^{2+}, Cd^{2+} and Yb^{3+} ions are chosen in this study) in strong alkaline medium is used to enhance the two-photon absorption (TPA) cross section (δ) of the material, which is useful for two-photon microscopy imaging in living HepG2 cells.

2 Experimental Section

2.1 Synthesis of L

All chemicals used were of analytical grade. All solvents were purified by conventional methods before use. The synthesis route of **L** was listed as **Scheme 1**.

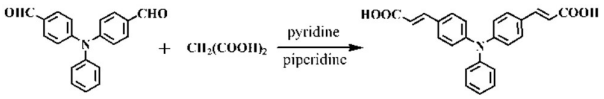

Scheme 1 Synthetic route of the target compound **L**

For preparing **L**, 4,4'-(phenylazanediyl)dibenzaldehyde (the preparation procedure was listed in †ESI, 0.5 g, 1.66 mmol) and malonic acid (0.357 g, 3.43 mmol) were dissolved in pyridine (5 mL) and 3-5 drops of piperidine was added as a catalyzer. The above mixture was refluxed for 4 h and monitored by TLC to ensure complete reaction. Then, water was added to the mixture and the pH value of the solution was adjusted to 5-6, then the precipitate was purified through recrystallization in ethanol to get a yellow solid. Yield: 85%. ^{1}H-NMR (400 MHz, d_6-DMSO): δ (ppm): 12.26 (s, 2H); 7.61(d, 4H, J = 8.8 Hz); 7.53 (d, 2H, J = 15.8 Hz); 7.39 (t, 2H); 7.19 (t, 1H, J = 7.2 Hz); 7.12 (d, 2H, J = 7.6 Hz); 6.99 (d, 4H, J = 8.8 Hz); 6.39 (d, 2H, J = 15.8 Hz). ^{13}C-NMR (100 MHz): δ (ppm) 167.73, 148.22, 145.84, 143.29, 129.93, 129.64, 128.61, 125.79, 124.89, 122.82, 117.23. FT-IR (KBr, cm^{-1}): ν = 3466 (m, ν_{COO}), 2978, 1679 (s, $\nu_{C=O}$), 1621 (s, $\nu_{C=C}$), 1591 (s), 1505 (s), 1423 (m), 980 (m), 834 (m), 698 (s), 763 (m), 701 (m).

Single crystals of **L** suitable for X-ray diffraction were obtained by slow evaporation of dichloromethane-methanol mixed solution (V_{CH2Cl2} : $V_{ethanol}$ = 2:1) at room temperature for a week.

2.2 Preparation of L nanostructures

L nanostructures were prepared through a simple reprecipitation process. For studying the effect of solvent on the aggregated style of **L**, 200 μL of **L** solution in different solvents (1.0×10^{-3} mol/L) was injected into 2 mL of high-purity water under stirring. The samples were stirred for 10 min and then left undisturbed for 12 h at room temperature for stabilization.

For studying the effect of acidity on the aggregation, 200 μL of **L**-THF solution (1.0×10^{-3} mol/L) was injected into 2 mL of water with different acidity, stirred for about 10 min and then left undisturbed at room temperature. To avoid the influence of other features on the morphology of **L**, the acidity of the solution was adjusted just through adding different amount of HCl or NaOH.

2.3 Preparation of coordination polymer particles

In this study, Ba^{2+}, Cd^{2+} and Yb^{3+} ions were chosen to prepare Ba-**L** CPPs, Cd-**L** CPPs and Yb-**L** CPPs. For synthesis of Ba-**L**, 50 μL of NaOH-ethanol solution (2.0×10^{-3} mol/L) was added to 5 mL of **L**-ethanol solution (1.0×10^{-5} mol/L). The mixture was stirred for about 30 min at room temperature. Then, 50 μL of Ba^{2+} aqueous solution (1.0×10^{-3} mol/L) was added and a large amount of precipitate occurred immediately [25]. After stabilizing for 10 min, the precipitate was collected by centrifugation, washed several times with ethanol and water alternately, and then dried under vacuum.

To prepare Cd-**L** and Yb-**L**, similar procedure was followed except that the metal salt of Ba^{2+} was changed to Cd^{2+}, Yb^{3+}, respectively. The products were characterized through FT-IR and powder XRD.

2.4 Cell culture, incubation and 2PFM imaging

In this study, human liver cancer cell (HepG2) was chosen as the testing candidate, which was cultured and stained with the organic nanomaterial and the corresponding Yb-**L** CPPs. HepG2 cells were seeded in 6 well plates at a density of 2×10^5 cells per well and grown for 96 hours. For live cell imaging, cell cultures were incubated with the materials at PBS solution (10% PBS: 90% cell media, PBS = phosphate buffered saline) at a concentration of 10 μM and maintained at 37 ºC in an atmosphere of 5% CO_2 and 95% air for incubation times ranging up to 60 min. The cells were then washed with PBS (3 × 3 mL per well) and imaged using confocal laser scanning microscopy with water immersion lenses.

HepG2 cells were fluorescence imaged on a Zeiss LSM 710 META upright confocal laser scanning microscope using 40 × magnification water-dipping lenses for the monolayer cultures. Image data acquisition and processing were performed using Zeiss LSM Image Browser, Zeiss LSM Image Expert and Image J.

2.5 TD-DFT calculation

Molecular orbital calculations of time-dependent density functional theory (TD-DFT) at the B3LYP/6-31g level basis set (Gaussian 03) [26] were performed to study the electronic structures and the corresponding energy gap of **L** molecules in different acidity. The molecular geometry used for the calculation was obtained from X-ray diffraction crystallographic data, protonated and/or deprotonated molecule structure.

2.6 Instrument

The pH value of the solution was adjusted by adding hydrochloric acid or sodium hydroxide in tetrahydrofuran-water mixture and determined with the pH meter of PHS-3CT. The X-ray diffraction measurement of single crystal was performed on a Bruker SMART II CCD area detector using graphite-monochromated Mo Ka radiation (λ = 0.71073 Å) at 298(2) K. Intensity data were collected in the variable multi-scan mode. The structures were solved by direct methods and difference Fourier syntheses. All non-hydrogen atoms were refined anisotropically and hydrogen atoms were introduced geometrically. Calculations were performed with the SHELXTL-97 program package [27]. The powder X-ray diffraction (PXRD) patterns were recorded on a MXP18AHF diffractometer using Cu Ka radiation (λ = 1.54056 Å) in the 2θ range from 8° to 40°. The morphologies were obtained on a field-emission scanning electron microscope (FESEM, Hitachi S-4800) and electron microscope (TEM, JEM-2100). UV-vis absorption spectra were obtained on a UV-3100 spectrophotometer in the wavelength range 200-800 nm. Fluorescence spectra were measured at room temperature using a Hitachi F-7000 spectrophotometer. The electrochemical tests were recorded on a CHI660D workstation. Voltammograms were recorded using a Pt disc working electrode in DMF containing 0.1 M Bu_4NClO_4 (TBAP). Scans started at 1.8 V versus a saturated calomel electrode (SCE), increasing at a rate of 50 mV/s.

2.7 Nonlinear optical measurements

The nonlinear optical properties of **L** and three CPPs were measured through Z-scan and two photon excited fluorescence measurements with a concentration of 1.0×10^{-4} mol/L (based on Mol. Wt. of **L**) using femtosecond laser pulse and Ti:95 sapphire system (80 MHz, 140 fs). For Z-scan measurements, the quartz-glass cell was 1.0 mm thick, and the average laser power was 120 mW. The optical path length for Z-scan was 5.0 cm from the sample. The excited wavelength was between 680 nm and 980 nm. For two photon excited fluorescence experiments, the quartz-glass cell was 1.0 cm thick and the average laser power was 500 mW.

Nonlinear absorption coefficient β was measured by open aperture Z-scan technique. For the open aperture, the normalized transmittance as a function of the position along the *z* axis can be calculated as **equation 1**

$$Tz = \sum_{m=0}^{\infty} \frac{[-q(z)]^m}{(m+1)^{3/2}}, \text{ where } q(z) = \frac{\beta I_0 L_{eff}}{[1+(z/z_0)^2]\alpha} \qquad (1),$$

where Z_0 is the diffraction length of the beam, I_0 is the intensity of the light at focus, L_{eff} is the effective length of the sample, and α is the linear absorption coefficient at the wavelength used.

Further, the molecular 2PA cross-section (δ) could also be determined through Z-scan measurement by using the following relationship, **equation 2**,

$$\delta = h\upsilon\beta \times 10^{-3}/N_A d, \qquad (2),$$

where *h* is the Planck's constant, *υ* is the frequency of input intensity, N_A is the Avogadro constant, and *d* is the concentration of the sample [28].

3 Results and Discussions

3.1 Effect of solvent on the self-assembly process of L

L nanostructures were simply prepared in several solvents (tetrahydrofuran THF, N,N-dimethyl formamide DMF, ethanol EtOH, acetone, acetonitrile were used in this study) with no addition of any surfactant, template or catalyst [29], the SEM images of which are shown in **Fig. 1**. The results revealed remarkable solvent-induced morphological change of **L**. When **L** molecules were introduced into THF-H_2O mixed solvent, rhombus-like morphology was observed as shown in **Fig. 1a**, the TEM image of which was shown in †ESI **Fig. S1**. The average sizes of the two diagonals were 5 μm and 1 μm, respectively. Moreover, it was noteworthy that each rhombus-like nanostructure contained two rhombic-layers sticking together closely with the thickness being about 500 nm. When DMF-H_2O was used as the solvent, flexible nanowires about several micrometers long and ~100 nm wide were observed as shown in **Fig. 1b**. However, the main products prepared from EtOH-H_2O (**Fig. 1c**) and acetone-H_2O (**Fig. 1d**) were rectangular structures with ~100 nm in diameter. What's more, spherical nanoparticles with size of about 100 nm were observed from acetonitrile-H_2O mixture (**Fig. 1e**). The results revealed that the nanostructure formation of **L** had a strong relationship to the solvent used, which can be attributed to the different strength of noncovalent intermolecular interactions between **L**-**L** molecules and **L**-solvent [30]. When ethanol, acetone, DMF and acetonitrile were used, the strength of weak interactions between **L**-solvent (such as hydrogen bond) was much high that can

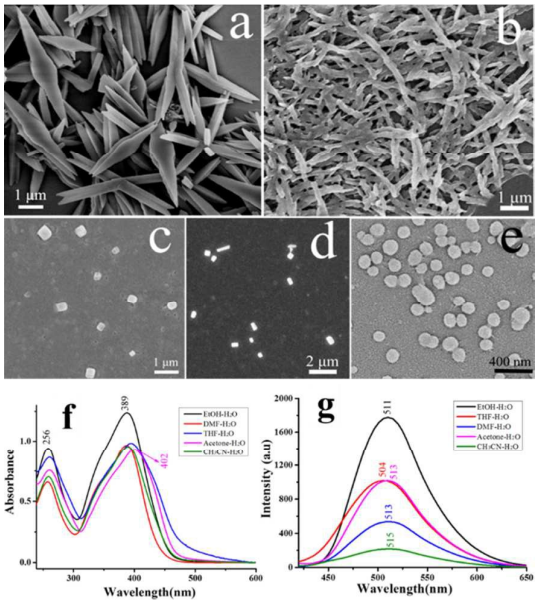

Figure 1. The morphologies of **L** prepared from different solvents: (a) THF-H_2O, (b) DMF-H_2O, (c) EtOH-H_2O, (d) acetone-H_2O and (e) acetonitrile-H_2O; (f) UV-vis spectra and (g) fluorescence spectra at

room temperature of **L** nanostructures prepared from different five solvents in this study.

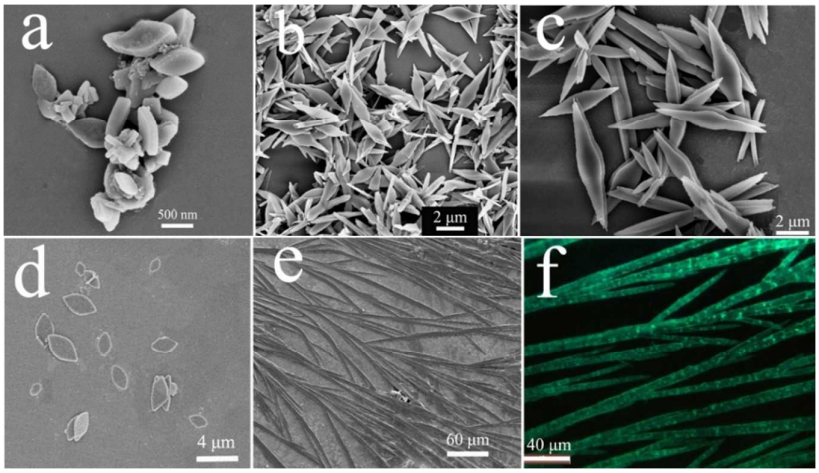

Figure 2 (a)-(e): SEM images of **L** nanostructures prepared in THF-H_2O solution of (a) pH = 1.0; (b) pH = 3.0; (c) pH = 5.0; (d) pH = 9.0 and (e) pH = 13.0; (f) Fluorescence microscopy image of **L** nanostructures in pH = 13.0

compete with the interactions between adjacent **L**-**L** molecules, which resulted in smaller size of the structures. When THF was used, the interaction strength between **L**-solvent was weaker (may be due to the weak dielectric constant of THF) that brought about somewhat larger size.

3.2 UV-vis absorption and Fluorescence properties of L nanostructures obtained from different solvents

As is known that nanomaterials with different morphologies are promising candidates to exhibit different optical properties due to different modes of molecular stacking [15, 31]. In this study, the solvent changed not only the self-assembly process of **L** molecules but also the linear optical properties. The UV-vis absorption and fluorescence properties of **L** nanostructures obtained from different five solvents mentioned above were studied and the results were shown in **Figure 1f** and **1g**.

All of the samples prepared from different solvents exhibited two major absorption peaks at around 255 nm and 400 nm with slightly shift (**Fig. 1f**). The former one peak with higher energy corresponded to the transition of the triphenylamine group, while the latter with lower energy resulted from the π-π* transition of the whole **L** molecule [32] accompanied by the intramolecular charge transfer effect. When different solvent was used, the transition of the triphenylamine group changed little while the band at lower energy was influenced more obviously. The nanowires obtained from DMF-H_2O showed the main absorption band at 387 nm. The main absorption band of rectangular-like nanostructures obtained from EtOH-H_2O and acetone-H_2O solvents were centered at 389 nm and 402 nm, respectively. The spherical nanoparticles from acetonitrile-H_2O showed a main absorption band at 390 nm. The nanorhombus obtained from THF-H_2O showed the main absorption band at 395 nm. The strength of the interactions between **L** and solvent molecules, the solvent effect, the morphology, the size and the corresponding size distribution may be the main causes of the changeable absorption phenomenon. The results also revealed that the solvents influenced the ICT process of **L** in some extent at nanometer scale.

Except for the UV-vis absorption, the fluorescence emission spectra of **L** nanostructures obtained from the five solvents also showed a slight shift as shown in **Fig. 1g**. The fluorescence of **L** nanorhombus prepared from THF-H_2O showed a green emission, the band of which centered at about 504 nm. The emission band centered at 511 nm, 513 nm, 513 nm and 515 nm for rectangular-like nanostructures obtained from EtOH-H_2O, nanowires obtained from DMF-H_2O, rectangular-like nanostructures from acetone-H_2O, and spheres from acetonitrile-H_2O, respectively. This phenomenon can be attributed to different strength of weak interactions between neighbouring molecules [33] in different solvents as discussed previously.

3.3 Effect of acidity on the self-assembly process of L

Except for the influence of solvents on the **L** morphology, the acidity of the solution changed the self-assembly process of **L** molecules more obviously to some extent, which was reasonable that **L** was a carboxylic acid derivative [34]. In order to study the influence of the solution acidity on the morphology, experiments were conducted by adjusting the pH value of the solution just adding HCl and/or NaOH into the system. Owing to the fact that the morphology of **L** nanostructures obtained from THF-H_2O mixture was more regular and interesting than that from the others, the following experiments were carried out in THF-H_2O mixture with different acidity while keeping the other conditions unchanged.

When **L** was introduced to weak acid solution of pH = 5.0, the rhombic-like morphology had little changed (**Fig. 2c**) and the morphology was similar to that obtained from pure THF-H_2O solution. When the acidity increased to pH = 3.0, the rhombic-like structure was also observed (**Fig. 2b**) with the longer diagonal of the rhombus decreased to about 3 μm. However, the two rhombic-layers structure was not easily observed and the thickness was decreased to about 100 nm. When the acidity reached to pH = 1.0, bread-like rhombic particles was observed, the size of which was

smaller than the samples obtained in other acid solution. The longer diagonal was ca. 600 nm, the shorter diagonal was ca. 400 nm and the thickness was about 200 nm (**Fig. 2a**). Similar morphology was

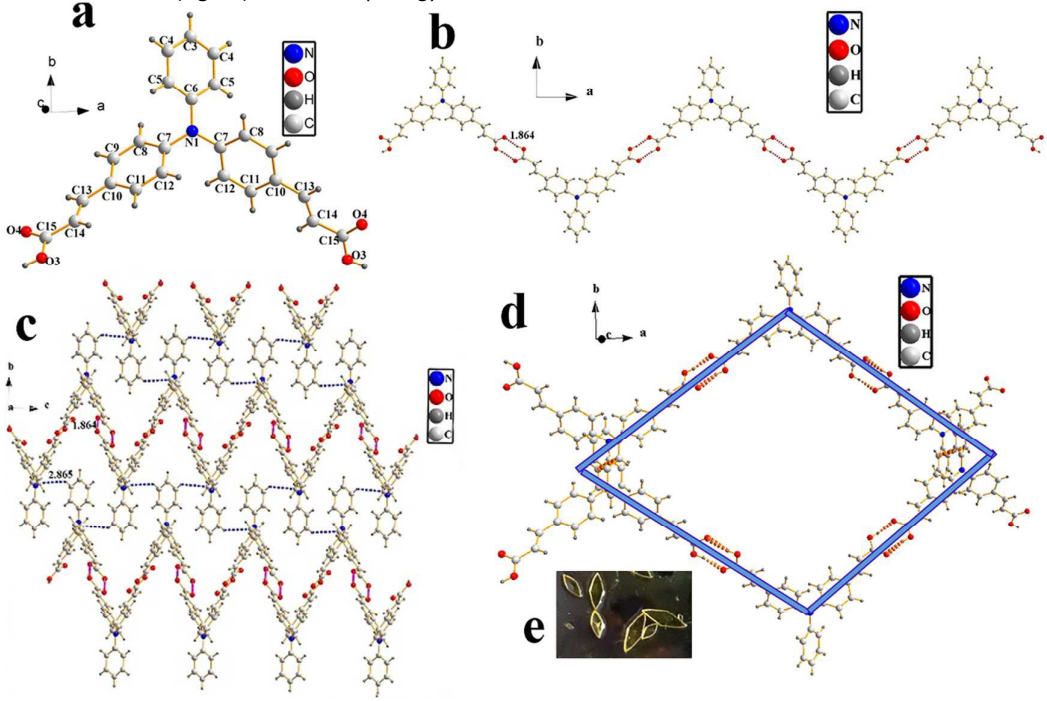

Figure 3 (a) Crystal structure and intermolecular interactions of **L** with the atom numbering scheme; (b) the one dimensional framework showing the weak O-H···O (red) hydrogen bonds along *a* axis at a distance of 1.864 Å; (c) the two dimensional architecture was connected by O-H···O (red) hydrogen bonds and C-H···C weak interactions at a distance of 2.865 Å; (d) the structure clearly showed the intermolecular interactions along *ab* plane; (e) crystal photographs of **L**.

Table 1 Crystal data and structure refinement for **L**

Compound	L	b [Å]	14.740(5)
Empirical formula	$C_{24}H_{19}NO_4$	c [Å]	8.691(5)
formula weight	385.40	α [deg]	90.000(5)
temperature (K)	298(2)	crystal system	orthorhombic
space group	*Pcca*	V [Å^3]	2023.2(15)
Z	4	μ [mm^{-1}]	0.086
D_{calcd} [g·cm^{-3}]	1.265	GOF	1.081
F (000)	808	Completeness to theta = 27.48	97.9 %
Crystal size (mm)	0.30 × 0.20 × 0.20	θ range [°]	1.38-25.00
Final R indices [I>2sigma(I)]	R_1 = 0.0432,	Reflections collected / unique	11431 / 1759
	wR_2 = 0.1342		[R(int) = 0.0401]
a [Å]	15.793(5)	R indices (all data)	R_1 = 0.0556,
			wR_2 = 0.1505

captured from TEM microscope as shown in ESI **Fig. S2**. The phenomenon may be due to the protonation effect caused by the interactions between hydrogen ion and carboxylic unit. The more the hydrogen ions existed, the stronger protonation effect and the hydrogen bonds formed, which brought about the stronger interactions between **L**-solvent and decreased the size of the morphology to much smaller.

On the other hand, **L** nanostructures obtained from alkaline medium were quite different from that obtained under acid medium and/or from pure THF-H_2O solution. When studied in the weak alkaline solution of pH = 9.0, the number of rhombus decreased significantly and the two rhombic-layers structure disappeared (**Fig. 2d**), which may be due to the erosion effect caused by the interactions between alkali and carboxylic unit. When **L** was put into strong alkaline medium of pH = 13.0, one-dimensional microwires with tiny branches were obtained, the length of which was several hundred micrometers and the average width was ~8 μm (**Fig. 2e**). The microwires emitted strong green light under the fluorescence microscope (**Fig. 2f**). A more interesting phenomenon was that a glaring light emission was observed at the node points of the microwires, indicating that the as-prepared microwires possessed optical waveguide effect [35]

when operated in the light transmission process. The corresponding TEM image shown in ESI **Fig. S3** clearly confirmed the node points.

3.4 Mechanisms of molecular stacking model

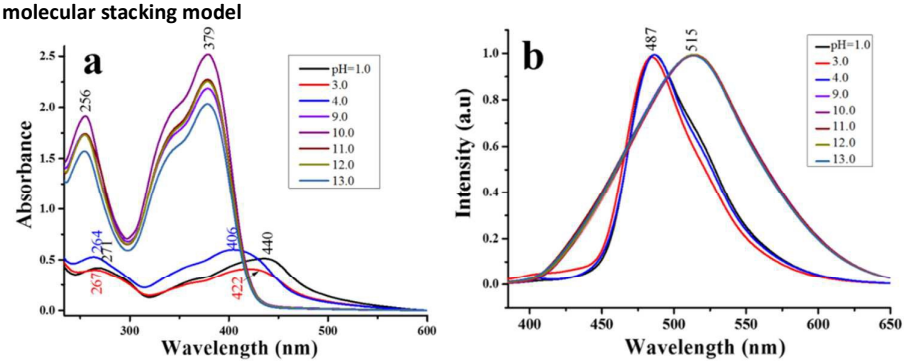

Figure 4 (a) the UV-vis absorbance, (b) normalized fluorescence spectra of **L** nanostructures obtained from THF-H_2O mixed solution under different pH value

morphologies prepared from different solvent and the acidity of the solution, the weak intermolecular interactions between adjacent **L** molecules were studied through single crystal of **L**.

L crystallized in orthorhombic form with space group *Pcca* as shown in **Figure 3**. The crystallography data were summarized in **Table 1**. Selected bond lengths and bond angles were listed in †ESI **Table S1**. In the molecule, the bond lengths were all of aromatic character. The linkage bond length between the benzene ring and the two carboxyl groups were quite conjugated with C10-C13 being 1.467(2) Å and C14-C15 being 1.470(2) Å. The C13=C14 double bond was nearly coplanar to the adjacent benzene and carboxyl group with the torsion angle of C9-C10-C13-C14 being 169.40º and O4-C15-C14-C13 being 176.58º. The structural features suggested that all nonhydrogen atoms were highly conjugated, which would benefit electronic delocalization in the whole molecule.

There was a O3-H3···O4 intermolecular hydrogen bond with the H3···O4 distance of 1.864 Å (C–H···O = 168.67 º) [36], which was the main driving force to form one-dimensional structure along *a* axis as shown in **Fig. 3b**. The adjacent molecules were also stacked through C-H···C weak interactions along *c* axis at a short intermolecular distance being 2.865 Å, which was very important in supramolecular crystal packing to form two-dimensional sheets in the *bc* plane as shown in **Fig. 3c**. There also existed weak π-π interactions as shown in the ESI **Fig. S4**. All these weak interactions were supposed to be the driving forces for the molecules self-assembly to construct bulk materials and/or micro/nanostructures.

When **L**-THF solution was injected into pure water, the limited solubility of **L** in water induced molecular segregation from THF and precipitation in water to form tiny seed crystals. Then, in the subsequent growth process, the intermolecular interactions between adjacent **L** molecules [37] acted as the driving force for the stacking of **L** molecules. These weak intermolecular interactions drove **L** molecules to align orderly and assemble mainly along two different directions as shown in **Fig. 3d**. There also existed O(**L**)-H(**L**)···O (THF or water) and/or O(water)-H(water)···O(**L**) interactions between **L** molecules and THF-H_2O solvent, together with the C-H···C weak interactions and weak π-π interactions, which were considered as the driving force for forming two rhombic-layers structure.

In order to better understand the relationship between the

When the **L** molecules were introduced into the THF-H_2O mixture with different acidity, the intermolecular interactions between **L**-**L** and/or **L**-solvent were changed [38]. When the molecules were injected into the acid solution, the carboxylic acid unit of **L** was protonated. Thus, the hydrogen bond between the carboxyl units of **L** and the solvent would be strong. The process would decrease the probability of the formation of O-H···O hydrogen bonds between **L**-**L** molecules. In the strong acidic environment (such as pH = 1.0), the hydrogen bond between the carboxyl groups of **L** and the solvent was somewhat stronger than that between **L**-**L** molecules, thus the molecules assembled to the smaller and thinner rhombic morphology, and the rapid growth of crystal seeds made it hard to form two rhombic-layers structure.

However, when the environment changed to alkaline condition, the carboxyl unit was expected to be deprotonated, which caused the intermolecular hydrogen bond between **L**-**L** molecules and **L**-solvents weakened and even disappeared. Thus, the formation of two-dimensional planar structure lost its driving forces. The C-H···C and π-π weak interactions became dominant in the molecular self-assembly process, resulting in more obviously one dimensional orientation growth [39] as shown in **Fig. 3e** and **f**.

3.5 Effect of acidity on the optical properties of L nanostructures

The acidity of the solution changed not only the self-assembly process of **L**, but the linear optical properties of it as well due to the existence of the two carboxyl units. The results of linear optical properties of **L** nanostructures prepared from different acidity was listed in **Fig. 4**. As shown in **Fig. 1f**, in pure THF-H_2O mixed solvent, the main absorption band of **L** centered at 257 nm and 395 nm. In acid solution, the absorption band red-shifted as shown in **Fig. 4a**. When the pH value was 4.0, the main absorption band centered at 406 nm, which red-shifted for about 11 nm from that of pure THF-H_2O solution. When the acidity of the solution increased, the extent of red-shift extended. When the pH value decreased to 3.0, the main band centered at 422 nm which red-shifted for about 27 nm from that of pure THF-H_2O solution, while it centered at 440 nm as pH = 1.0 which showed a red-shift for about 45 nm. The lower the pH value, the larger the red-shifted wavelength. However, when **L**

molecules were under alkaline conditions, the main absorption band centred at about 379 nm till the value increased to pH = 13.0.

The phenomenon may be caused from the deprotonation and/or protonation effect of **L** molecules. When pH value was 1.0, the whole molecule was thoroughly protonated, the existence of protonated carboxyl unit enlarged the strength of acceptor unit, which caused the increased strength of D-A pairs, and brought about red-shifted absorption. As a result, the band at 440 nm red shifted for about 45 nm from 395 nm under pure THF-H_2O mixture. When the pH value increased, the protonation effect weakened, the red-shifted degree of absorption band decreased along with it till the band centered at about 406 nm as pH = 4.0. On the contrary, when the whole system was under alkaline environment, the deprotonation effect controlled the molecule and the whole molecule existed as alkaline structure. The strength of D-A pairs was weakened and the absorption band centered at 379 nm which showed a 16 nm blue-shift from that of pure THF-H_2O solution. The shifted absorption was further researched through theoretical study as shown in part 3.6.

The fluorescence emission also revealed shifted phenomenon as shown in **Fig. 4b**. When the system was in acid environment, the main fluorescence emission band existed at 487 nm, while it centred at ~515 nm when the material was under alkaline condition. The possible reason was also attributed to the deprotonation and/or protonation effect of **L** molecule. The different stacking mode of the molecules under acidic and/or alkaline conditions (as discussed previously) resulted in the different shifted trend.

3.6 Theoretical calculation

To better understand electron structure of **L** and the electron absorption under different acidity conditions, the ICT process was interpreted directly by the theoretical calculations on the energy levels, which were performed by time-dependent density functional theory (TD-DFT) calculation method at B3LYP/6-31g level based on the **L** molecule conformation in the crystal structure [40], deprotonated and protonated structures. The calculated results and the spatial distributions of the corresponding molecular orbital diagrams were listed in **Fig. S5-S8**.

As for **L** molecules, compared with the distribution plots of the highest occupied molecular orbital (HOMO), the electrons of the lowest unoccupied molecular orbital (LUMO) were distinctly different as shown in ESI **Fig. S5**. The electron cloud density in the HOMO of **L** was mainly concentrated on the electron-donating triphenylamine moiety with low coefficients on the electron-withdrawing carboxylic groups. In the LUMO, the electrons were mainly concentrated on the carboxylic unit and its adjacent benzene ring. There was low electron density distribution on the benzene ring far away from the carboxyl unit. The separation between HOMO and LUMO indicated that substantial charge transferred from the donor moiety to the acceptor moiety when the molecules were excited. The theoretical calculated band gaps between HOMO-1 and LUMO was 3.1423 eV with f = 0.69683, which equalled to 394.56 nm and fit with the UV-vis experimental results. In the HOMO-1 orbit, the electrons are primarily concentrated on the C=C double bond and the benzene rings near the two carboxyl units. Obviously, the electron transition from the HOMO-1 to the LUMO was accompanied by intramolecular charge transfer from the central triphenylamine moiety to the peripheric carboxyl unit.

When **L** molecules were thoroughly protonated in strong acid environment, the theoretical calculation results revealed that the main absorption band gap was 2.7457 eV (that was 451.55 nm) with f = 1.0481, which was excited from HOMO-2 to LUMO orbit as shown in **Fig. S6**. In the HOMO-2 orbit of the protonated **L** molecule, the electrons were primarily concentrated all around the molecule. In the LUMO, the electrons are primarily concentrated on the carboxylic unit and its adjacent benzene ring. When **L** molecules were partly protonated in weak acid environment, the calculated main absorption band gap was 2.9430 eV (that was 421.28 nm), which was excited from HOMO to LUMO orbit (shown in **Fig. S7**).

When **L** was deprotonated to be carboxylic acid anion, the charge transfer process was significant changed as shown in **Fig. S8**. The theoretical calculation results revealed that the main absorption band gap was 3.2377 eV with f = 0.61247, the corresponding wavelength equalled to 382.93 nm, which was from HOMO-4 to LUMO orbit. In the HOMO-4 orbit, the electrons are primarily concentrated on the carboxylic units. In the LUMO, the electrons are mainly concentrated on the oxygen atoms of carboxylic units. The changing structure of the electron cloud density in different conditions may bring about the changeable optical properties.

3.7 The preparation and morphology of coordination polymer particles

The results discussed above revealed that the solvent and solution acidity influenced the weak intermolecular interactions, the self-assembly process, the molecular stacking mode and the corresponding linear optical properties of **L** nanostructures. Further, the next main purpose of this study was to research the coordination effect between **L** molecule and metal ions on the stacking mode and the corresponding optical properties. Through the intermolecular interactions between metal ions and carboxylic acid units of **L** molecule, size- and morphology-dependent nanoparticles can be obtained. Among the numerous alternative metal ions, three metal salts, Ba^{2+}, Cd^{2+} and Yb^{3+}, were chosen considering the outer electron structure, the possible coordination number and the fluorescence of **L** under the existence of metal ions (shown in ESI **Fig. S9**). There were some factors that played vital roles in affecting the morphology of the resulting CPPs, such as the amount of solvent, the molar ratio of reactants used in the reaction, the additives for adjusting the deprotonation rate, et al [13, 41]. To reduce these influence factors, the solvent was the same as that used when described in part 3.3, which was THF-H_2O mixed solvent with the water fraction fw = 90%. The amount of metal ions to **L** was fixed at 1:1 and NaOH was used to deprotonate **L** molecules, which can maximize the protonation speed. Thus, three CPPs, Ba-**L**, Cd-**L** and Yb-**L**, were prepared through the coordination process between **L** and Ba^{2+}, Cd^{2+} and Yb^{3+} ions, respectively.

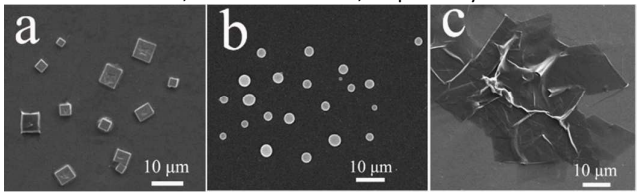

Figure 5 SEM images of coordination polymer particles (a) Ba-**L**, (b) Cd-**L** and (c) Yb-**L** obtained by dispersing the samples in ethanol.

These three CPPs were analysed through infrared spectroscopy (ESI **Fig. S10**) and powder X-ray diffraction (ESI **Fig. S11**), the results of which revealed the intermolecular coordination effect between **L** molecule and these different metal ions, which also confirmed the formation of CPPs. In infrared spectroscopy, the C-O stretching frequency at 1680 cm^{-1} for uncoordinated **L** shifted to ~1634 cm^{-1} for the three CPPs, which illustrated the complete deprotonation of the carboxylate unit after the formation of these CPPs.

The morphology of these three CPPs was studied through SEM and TEM analysis as shown in **Fig. 5** and **Fig. S12-S13**, respectively. The rectangular microcubes with clear surface of Ba-**L** were observed with the average size of the length being 3-7 μm (**Fig. 5a** and **Fig. S12**). Spherical nanoparticles of Cd-**L** with diameter varied from 100 nm to 300 nm were observed as shown in **Fig. 5b** and **Fig. S13**. While for Yb-**L**, silk-like structures with the size of about dozens of micron were observed as shown in **Fig. 5c**. The results indicated that the morphology had strongly associated to the metal ions used. As Ba^{2+} interacted with **L** through the two carboxylic units, the O-H···O hydrogen bonds between **L** molecules disappeared, which resulted in the disappearing of the main driving forces of the rhombic morphology formation. The newly existed intermolecular interactions amongst Ba-**L** molecules drove them stacked into rectangular structure [42], which can also be considered as the distorted rhombic morphology. That was to say, the introduction of Ba^{2+} ion changed the morphology slightly. When Cd^{2+} was introduced into the synthetic system with the coordination number of Cd^{2+} being about 4 or 6, the increased number of **L** molecules led them uniformly distributed around the centre core Cd^{2+} ions. Thus, the differences of the intermolecular interactions between adjacent Cd-**L** molecules along three dimensions were small, which resulted in the spherical nanoparticles. Further, as Yb^{3+} ions were introduced, whose coordination number was high to about 8 to 12, there would be several **L** molecules attached to the centre core Yb^{3+} ions. Thus, the steric hindrance led the weak crystallinity of Yb-**L** molecules and the growth along three dimensions was difficult which brought about the formation of two dimensional silk-like morphology with low crystallinity.

3.8 Optical properties of the as-prepared three CPPs

The construction of CPPs brought about not only the changeable morphology, but also the optical phenomena, linear and nonlinear optical properties included.

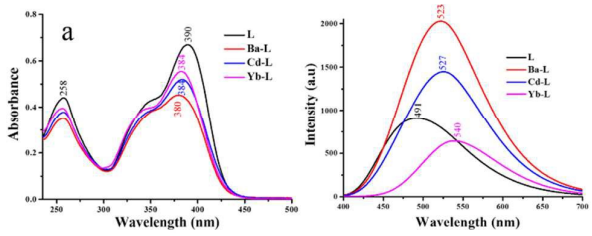

Figure 6 (a) UV-vis spectra and (b) single photon fluorescence spectra of **L** and three CPPs dispersed in ethanol solution as the concentration being 1.0×10^{-3} mol/L

3.8.1 Linear optical properties

The UV-vis absorption and single-photon-excited fluorescence emission of **L** and three CPPs were studied and compared as shown in Fig. 6. The UV-vis absorption spectrum of **L** in ethanol solution exhibited two major absorption bands centred at 258 nm and 390 nm, respectively. The absorption band of the three corresponding CPPs showed slight blue-shift to about 383 nm. There were also some differences in the emission wavelength of **L** and the CPPs. **L**-EtOH solution exhibited a green-blue emission centred at 491 nm. The Ba-**L** and Cd-**L** CPPs showed the main emission band at 523 nm and 527 nm, respectively, the fluorescence of which was higher than that of pure **L**-ethanol solution. On the other hand, Yb-**L** showed a green emission centred at 540 nm, which was weaker than that of pure **L**-ethanol solution. The possible reason of the red-shifted fluorescence emission for the three CPPs may be attributed to the organic linker chelating to the metal centre, which effectively increased the rigidity of the ligand and further enhanced the ICT process of the ligand molecules.

3.8.2 Nonlinear optical properties

Except for the linear optical properties, **L** and the corresponding three CPPs exhibited excellent nonlinear optical properties. Through the open- and closed-Z-scan method, the sign and magnitude of the second- and third-order nonlinear optical susceptibilities of **L** and the three CPPs were measured, including the nonlinear refractive index (γ), nonlinear absorption coefficient (β), TPA cross section (δ), and third-order nonlinear susceptibility ($\chi^{(3)}$). The concentration of each sample was 1.0×10^{-4} mol/L. The two photon excited fluorescence was captured under the best TPA wavelength confirmed from the open-Z-scan experiment, which was 800 nm for **L**, 720 nm for Ba-**L**, 720 nm for Cd-**L** and 740 nm for Yb-**L** CPPs, respectively. The results were shown in **Figure 7**. The nonlinearity parameters for **L** and the CPPs were extracted and summarized in **Table 2**.

Two photon excited fluorescence

The two photon excited fluorescence (2PEF) spectra of the four samples are shown in top row of **Fig. 7**, respectively. The maximum emission wavelength located at 503 nm for **L**, 530 nm for Ba-**L**, 531 nm for Cd-**L** and 510 nm for Yb-**L**, respectively. The 2PEF peak position of the samples showed shift with different extents compared to that of 1PEF (see **Fig. 6b**), which was 12 nm red-shift for **L**, 7 nm red-shift for Ba-**L** and 4 nm red-shift for Cd-**L**, respectively. On the contrary, for that of Yb-**L**, the 2PEF peak position showed a 30 nm blue-shift from that of 1PEF. The results indicated the difference of the excited states for 1PEF and 2PEF, mainly during the excitation process: single-photon absorption *vs*. two-photon absorption [43].

Two photon absorbance

The second-order nonlinear optical susceptibilities of **L** and the three CPPs were measured through the open Z-scan method as shown in middle row of **Fig. 7**. Based on Equations (1) and (2), β of **L** at $I_0 = 1.115 \times 10^8$ GW·cm^{-2} was 0.003224 cm/GW and δ was 133.01 GM. Whereas, β of the Ba-**L** CPPs at $I_0 = 1.308 \times 10^8$ GW·cm^{-2} was 0.005076 cm/GW and δ was 232.65 GM, β of the Cd-**L** CPPs at $I_0 = 1.308 \times 10^8$ GW·cm^{-2} was 0.006306 cm/GW and δ was 289.06 GM,

and β of the Yb-**L** CPPs at I_0 = 1.238 × 10^8 GW·cm^{-2} was 0.01299 cm/GW and δ was 579.50 GM, respectively. Clearly, the TPA coefficient and TPA cross section of the three kinds of CPPs were larger than that of pure **L**. For TPA cross section, it increased approximately 1.75, 2.17, 4.35 times respectively. For Ba-**L**, the coordination effect can enlarge the π- conjugated degree of **L**

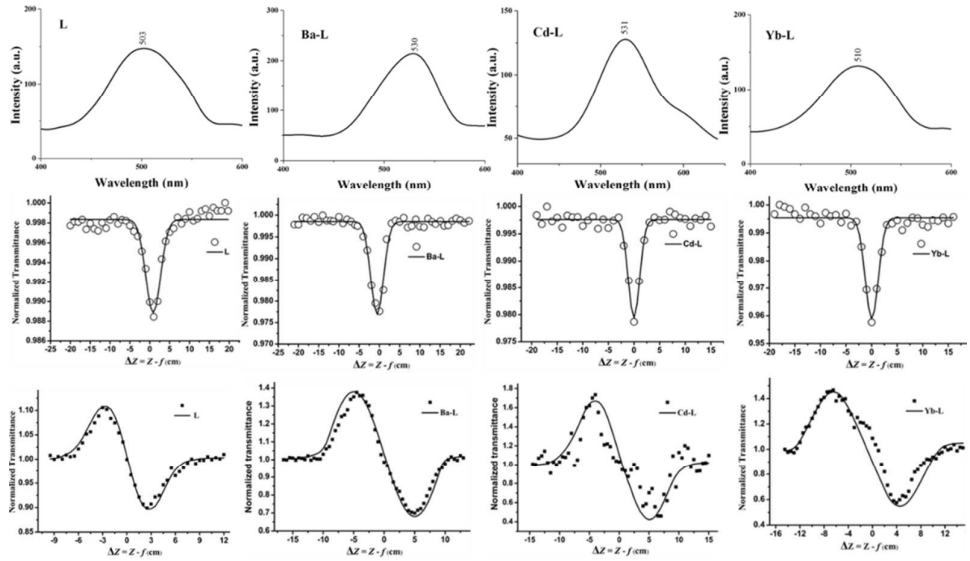

Figure 7 (up): two photon excited fluorescence; (middle): open-aperture Z-scan response curves (solid lines show fitting to experimental data); (down): close-aperture Z-scan response curves (solid lines show fitting to experimental data), for **L**, Ba-**L**, Cd-**L** and Yb-**L**, respectively.

Table 2 Open- and closed-aperture Z-scan measurement data for the nonlinearity parameters of **L** and the three CPPs

	L	Ba-**L**	Cd-**L**	Yb-**L**
wavelength [nm]	800	720	720	740
TPA coefficient β extrapolated to solute [cm/GW]	0.003224	0.005076	0.006306	0.01299
I_0 [GW/cm]	1.115 × 10^8	1.308 × 10^8	1.308 × 10^8	1.238 × 10^8
δ [GM]	133.01	232.65	289.06	579.50
γ[cm^2/W]	3.033 × 10^{-15}	5.107 × 10^{-15}	5.794 × 10^{-15}	4.597 × 10^{-15}
Re($\chi^{(3)}$) [esu]	-1.574 × 10^{-13}	-2.651 × 10^{-13}	-3.007 × 10^{-13}	-2.385 × 10^{-13}
Im($\chi^{(3)}$) [esu]	-1.039 × 10^{-8}	-1.510 × 10^{-8}	-1.897 × 10^{-8}	-3.973 × 10^{-8}

molecules, which caused the increased δ data [44]. While for Cd-**L** and Yb-**L**, except for the enlarged π-conjugated degree, the lager coordination number may bring about more ligand molecules around the centered metal ions, which resulted in increased δ data. The results fit with the discussions mentioned in part 3.7.

Third-order nonlinear susceptibility

For the closed aperture, the calculation of the nonlinear refractive index γ fitting can be done as in **Equation (3)**.

$$T_{P-V} = 0.406(1-s)^{0.25}|\Delta\Phi|, \text{ where } |\Delta\Phi| = KL_{\text{eff}}\gamma I_0 \quad \textbf{(3),}$$

where $\Delta T_{P\text{-}V}$ is the peak–valley transmittance difference from the closed-aperture scan. It can be seen that the difference between normalized transmittance values at valley and peak positions. The calculated nonlinear refractive indexes γ were 3.033 × 10^{-15} cm^2/W for **L** and 5.107 × 10^{-15}, 5.794 × 10^{-15}, 4.597 × 10^{-15} cm^2/W for Ba-**L**, Cd-**L** and Yb-**L**, respectively. It was clear that γ increased when the coordination polymer particles formed.

The third-order nonlinear susceptibility (Re($\chi^{(3)}$) was also determined through the closed-aperture Z-scan method. The value of the real part of the third-order nonlinear susceptibility, (Re($\chi^{(3)}$), can be calculated by the experimental measurements of γ as in **Equation (4)**

$$Re\chi^{(3)}(esu) = \frac{\varepsilon_0 c^2 n_0^2 \gamma}{\pi} \quad \textbf{(4),}$$

where ε_0 is the vacuum permittivity, c is the velocity of light in a vacuum, n_0 is the linear refractive index. The value of (Re($\chi^{(3)}$) was calculated to be -1.574 × 10^{-13} esu for **L**. As for the CPPs of Ba-**L**, Cd-**L**, Yb-**L**, the values were -2.651 × 10^{-13}, -3.007 × 10^{-13}, -2.385 × 10^{-13} esu, respectively, the values of which were all higher than that of pure **L**. The results indicated that the CPPs could reasonably be a better candidate for third-order NLO materials.

The value of the imaginary part of the third-order nonlinear susceptibility, Im($\chi^{(3)}$), can be calculated from the value of β as given in **Equation (5)**

$$Im\chi^{(3)}(esu) = \frac{\varepsilon_0 c^2 n_0^2 \lambda \beta}{4\pi^2} \quad \textbf{(5),}$$

Owing to the existence of coordination interactions between **L** and metal ions, an increase in Im($\chi^{(3)}$) value was expected. Indeed, the absolute value of Im($\chi^{(3)}$) of Ba-**L** CPPs, Cd-**L** CPPs, Yb-**L** CPPs were 1.510 × 10^{-8}, 1.897 × 10^{-8}, and 3.973 × 10^{-8} esu, respectively, all of which were higher than the absolute value of pure **L** (1.039 × 10^{-8} esu).

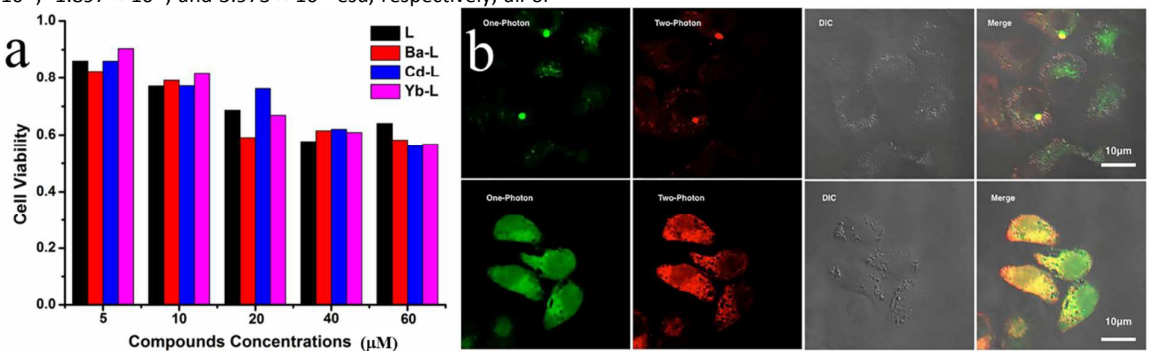

Figure 8 (a) MTT assay of HepG2 cells treated with **L** and/or the CPPs at different concentrations for 24 h; (b) one-photon image, Two-photon fluorescence microscopy (2PFM) image, Bright-field image of HepG2 cells stained with the samples and Merged image and of HepG2 cells incubated with: (upper) 10 μM of **L**, (down) 10 μM of Yb-**L** CPPs, after 60 min of incubation, washed by PBS buffer, with excitation at 800 nm and 740 nm, respectively.

It was known that the real part of $\chi^{(3)}$ led to an induced refractive-index change whereas the imaginary part was responsible for the two-photon absorption. In this study, the samples' absolute value of imaginary part of $\chi^{(3)}$ was larger than that of the real part. The ratio of imaginary part to real part was as large as 10^5. This meant that **L** and these CPPs possessed high TPA activity and could be a good TPA material for optical-limiting applications and/or protective devices.

3.9 Two-photon microscopy bio-imaging application

To evaluate the performance of the as-prepared material in live cells, a 2PFM imaging was conducted. Human liver cancer cells (HepG2) were the testing candidates, cultured and stained with the samples. The large 2PA action cross-sections of these samples made all of them suitable attractive candidates for two photon imaging. Here, the ligand **L** and Yb-**L** CPPs were chosen as the two photon imaging agents as the TPA cross section δ of Yb-**L** was the largest among these three CPPs.

3.9.1 Cytotoxicity tests (MTT assay)

Considering the application in two-photon fluorescence imaging, the MTT assay was performed at the first stage to ascertain the cytotoxic effect of **L** and the CPPs. Cytotoxicity is a potential side effect of dyes that must be controlled when dealing with living cells or tissues. In this study, all of the experiments were repeated three times. The measured data for each set of experiments were expressed with the average value. **Fig. 8a** showed the cell viability for HepG2 cells when different concentrations of the samples was used. The results clearly indicated that the cells incubated with **L** and the CPPs under the concentration of 5 μM remained about 85-90% viable after 24 h of feeding time, demonstrating the preferable biocompatibility. When the concentration of the samples was up to 60 μM, the viable cells gradually decreased to about 60%. The cytotoxicity tests definitely indicated that the low-concentration of the samples would not give rise to obvious toxic effects on living cells over a period of 24 h, which indeed have great potentials for further biological studies [45].

3.9.2 Two-photon microscopy bioimaging

Two-photon excitation cell imaging was achieved by using HepG2 cancer cells through two-photon laser scanning confocal microscopy (**Fig. 8b**). Treated cells were excited at a proper 2PA wavelength, which was 800 nm for the **L**, 740 nm for the Yb-**L**, respectively. The green channels in **Fig. 8b** showed 1PFM imaging. The red channels in **Fig. 8b** showed 2PFM imaging. These micrographs clearly revealed that the samples successfully internalised with HepG2 cells. Two-photon induced fluorescence was observed predominantly from the cellular cytoplasmic region, which was consistent with the images collected *via* 1PFM imaging [46]. Furthermore, the 2PFM image showed that after one hour incubation with HepG2 cells under low concentration (~10 μM), the Yb-**L** CPPs can widely and evenly uptake lysosome part all around the HepG2 cells. However, for **L**, only small parts of the lysosome were uptaken. Maybe the good biological compatibility of the Yb-**L** CPPs in this experiment caused the phenomenon. When **L** was introduced into the cell, bad biological compatibility of it resulted in less material entering and uneven distribution. On the contrary, after Yb-**L** CPPs were introduced, the biological compatibility increased, which led the whole CPPs uniformly introduced into the cytoplasm. The different biological compatibility of **L** and Yb-**L** CPPs can also be concluded from MTT results mentioned above when the concentration was 10 μM.

4 Conclusion

An A-π-D-π-A type organic ICT compound (**L**) was designed, synthesized and characterized. The effect of solvent, pH and existence of metal ions on the self-assembly morphology and the

corresponding optical properties was studied in detail. By self-assembly process, the rhombic nanoparticles were obtained from THF-H_2O mixed solvent and the morphology can be further tuned by changing the acidity of the growing solution. The changeable morphology further brought about tuneable optical properties. The possible mechanism was discussed through the single crystal structure and the theoretical calculation, which revealed that the morphology and the corresponding optical properties changed accordingly due to the different intermolecular interactions and the corresponding different molecular stacking styles at various environments. Further, **L** was liable to prepare coordination polymer particles through the strong interactions between carboxylic acid units and metal ions, which can also obtain size- and morphology-dependent nano/micro-particles. Moreover, the formation of CPPs brought about enhanced nonlinear optical properties, two-photon absorption cross section included, which made them suitable for two-photon microscopy bio-imaging application in living HepG2 cells. The increased biological compatibility of Yb-**L** made it suitable for uptaking lysosome part of HepG2 cells more widely and evenly.

Acknowledgements

This work was supported by the Natural Science Foundation of Anhui Province (1508085SMB208), the NSFC (No: 51432001), and the Educational Commission of Anhui Province of China (KJ2014ZD02).

Notes and references

† Electronic Supplementary Information (ESI) available: [Preparation of 4,4'-(phenylazanediyl)dibenzaldehyde; Selected bond lengths [Å] and angles [°] for **L**; The spatial distributions of calculated results; TEM images of CPPs and **L** nanostructures obtained under different pH values. Cyclic voltammograms of **L**; The FT-IR spectra of **L** and CPPs; The powder X-ray diffraction of **L** and CPPs.]. See DOI: 10.1039/b000000x/

‡ Crystallographic data reported in this manuscript were deposited with Cambridge Crystallographic Data Centre as supplementary publication No. CCDC-1440441. These data can be obtained free of charge via http://www.ccdc.cam.ac.uk/conts/retrieving.html, or email: deposit@ccdc. cam.ac.uk

1 (a) E. Ravindran and S. J. Ananthakrishnan, *J. Mater. Chem. C*, 2015, **3**, 4359; (b) L. Magginia and D. Bonifazi, *Chem. Soc. Rev.*, 2012, **41**, 211.
2 O. Fenwick, C. V. Dyck, K. Murugavel, D. Cornil, F. Reinders and S. Haar, *J. Mater. Chem. C,* 2015, **3**, 3007.
3 J. Y. Xiang, X. L. Cai, X. D. Lou, G. X. Feng, X. H. Min, W. W. Luo, B. R. He, C. C. Goh, L. G. Ng, J. Zhou, Z. J. Zhao, B. Liu, and B. Z. Tang, *ACS Appl. Mater. Interfaces*, 2015, **7**, 14965.
4 W. B. Zhang, L. B. Xing, H. S. Wang, X. J. Liu, Y. Q. Feng and C. Y. Gao, *Langmuir*, 2015, **31**, 4330.
5 X. F. Mei, G. X. Wen, J. W. Wang, H. M. Yao, Y. Zhao, Z. H. Lin and Q. D. Ling, *J. Mater. Chem. C*, 2015, **3**, 7267.
6 (a) C. Rest, R. Kandanelli and G. Fernández, *Chem. Soc. Rev.*, 2015, **44**, 2543; (b) G. Lu, Y. L. Chen, Y. X. Zhang, M. Bao, Y. Z. Bian, X. Y. Li and J. Z. Jiang, *J. Am. Chem. Soc.*, 2008, **130**, 11623.
7 F. S. Kim, G. Q. Ren and S. A. Jenekhe, *Chem. Mater.*, 2011, **23**, 682.
8 Y. Shi, D. Frattarelli, N. Watanabe, A. Facchetti, E. Cariati, S. Righetto, E. Tordin, C. Zuccaccia, A. Macchioni, S. L. Wegener, C. L. Stern, M. A. Ratner and Tobin J. Marks, *J. Am. Chem. Soc.*, 2015, **137**, 12521.
9 X. D. Liu, B. Z. Chen, X. J. Li, L. F. Zhang, Y. J. Xu, Z. Liu, Z. P. Cheng and X. L. Zhu, *Nanoscale,* 2015, **7**, 16399.
10 (a) X. Just-Baringo and D. J. Procter, *Acc. Chem. Res.*, 2015, **48**, 1263; (b) O. Ivasenko and D. F. Perepichka, *Chem. Soc. Rev.,* 2011, **40**, 191.
11 (a) W. Du, A. J. Cruz-Cabeza, S. Woutersen, R. J. Davey and Q. Yin, *Chem. Sci.*, 2015, **6**, 3515; (b) J. J. Benítez, J. A. Heredia-Guerrero, F. M. Serrano and A. Heredia, *J. Phys. Chem. C*, 2008, 112, 16968.
12 (a) W. Cho, H. J. Lee and M. Oh, *J. Am. Chem. Soc.*, 2008, **130**, 16943; (b) F. Nador, F. Novio and D. Ruiz-Molina, *Chem. Commun.*, 2014, **50**, 14570.
13 K. Wang, Y. Yin, C. Li, Z. Geng and Z. Wang, CrystEngComm, 2011, **13**, 6231.
14 X. Zhang, Z. K. Chen, and K. P. Loh, *J. Am. Chem. Soc.,* 2009, **131**, 7210.
15 A. K. Mahapatra, K. Maiti, S. K. Manna, R. Maji, S. Mondal, C. D. Mukhopadhyay, P. Sahoo and D. Mandal, *Chem. Commun.*, 2015, **51**, 9729.
16 H. J. Lee, W. Cho, S. Jung and M. Oh, *Adv. Mater.,* 2009, **21**, 674.
17 (a) Y. Lu, F. F. Xue, H. Yang, M. Shi, Y. P. Yan, L. J. Qin, Z. G. Zhou and S. P. Yang, *J. Phys. Chem. C*, 2015**, 119**, 573; (b) Y. -Y. Niu, Y. L. Song, J. Wu, H. Hou, Y. Zhu and X. Wang, *Inorg. Chem. Commun.*, 2004, **7**, 471; (c) O. R. Evans and W. Lin, *Acc. Chem. Res.*, 2002, **35**, 511.
18 (a) A. A. Karyakin, E. A. Puganova, I. A. Budashov, I. N. Kurochkin, E. E. Karyakina, V. A. Levchenko, V. N. Matveyenko and S. D. Varfolomeyev, *Anal. Chem.*, 2004, **76**, 474; (b) J. D. Qiu, H. Z. Peng, R. P. Liang, J. Li and X. H. Xia, *Langmuir*, 2007, **23**, 2133; (c) K. C. Naeem, A. Subhakumari, S. Varughese and V. C. Nair, *J. Mater. Chem. C,* 2015, **3**, 10225.
19 C. Fitzpatrick, E. Olivetti, T. R. Miller, R. Roth, and R. Kirchain, *Environ. Sci. Technol.*, **2015**, *49*, 974.
20 (a) A. Gross, H. Alborzinia, S. Piantavigna, L. L. Martin, S. Wölfl and N. Metzler-Nolte, *Metallomics,* 2015, **7**, 371; (b) G. Gunkel-Grabole, S. Sigg, M. Lomora, S. Lörcher, C. G. Palivan and W. P. Meier, *Biomater. Sci.*, 2015, **3**, 25.
21 (a) S. Lee, K. Park, K. Kim, K. Choi and I. C. Kwon, *Chem. Commun.*, 2008, 4250; (b) K. B Wang, Z. R. Geng, M. B. Zheng, L. Y. Ma, X. Y. Ma and Z. L. Wang, *Cryst. Growth Des.*, 2012**, 12**, 5606.
22 J. K. Augustine, Y. A. Naik, A. B. Mandal, N. Chowdappa and V. B. Praveen, *J. Org. Chem.*, 2007, **72**, 9854.
23 (a) M. D. Saban, L. D. Murphy, T. E. Enright, US 2008/0076049 A1; (b) L. D. Murpht, S. J. P. Robinson, Us 2007/0232830 A1.
24 S. P. Singh, M. S. Roy, K. R. J. Thomas, S. Balaiah, K. Bhanuprakash and G. D. Sharma, *J. Phys. Chem. C*, 2012, **116**, 5941.
25 K. B. Wang, Z. R. Geng, Y. X. Yin, X. Y. Ma and Z. L. Wang, *CrystEngComm*, 2011, **13**, 5100.
26 M. J. Frisch, G. W. Trucks, H. B. Schlegel, G. E. Scuseria, M. A. Robb, J. R. Cheeseman, et al. Gaussian 09, revision B.01. Wallingford CT: Gaussian Inc; 2010.
27 G. M. Sheldrick, SHELXTL V.51 Software Reference Manual, Bruker AXS, Inc., Madison, Wisconsin, USA, 1997.
28 L. Kong, J. X. Yang, S. L. Li, Q. Zhang, Z. M. Xue, H. P. Zhou, J. Y. Wu, B. K. Jin and Y. P. Tian, *Chem. Eur. J.*, 2013, **19**, 16625.

29 L. Kong, J. X. Yang, X. P. Hao, H. P. Zhou, J. Y. Wu, F.Y. Hao, L. Li, S. Y. Zhang, B. K. Jin, X. T. Tao, M. H. Jiang and Y. P. Tian, *J. Mater. Chem*., 2010, **20**, 7372.
30 (a) X. J. Zhang, X. H. Zhang, K. Zou, C. S. Lee and S. T. Lee, *J. Am. Chem. Soc*., 2007, **129**, 3527; (b) L. J. Prins, D. N. Reinhoudt and P. Timmerman, *Angew. Chem*. *Int. Ed.*, 2001, **40**, 2382.
31 J. E. Raymond, G. Ramakrishna, R. J. Twieg and T. GoodsonIII, *J. Phys. Chem. C*, 2008, **112**, 7913.
32 X. L. Tang, W. M. Liu, J. S. Wu, C. S. Lee, J. J. You and P. F. Wang, *J. Org. Chem*., 2010, **75**, 7273.
33 J. Wang, Y. F. Zhao, J. H. Zhang, J. J. Zhang, B. Yang, Y. Wang, D. K. Zhang, H. You and D. G. Ma, *J. Phys. Chem. C*, 2007, **111**, 9177.
34 P. Peng, Y. H. Wang, M. J. Rood, Z. Q. Zhang, F. Subhan, Z. F. Yan, L. H. Qin, Z. H. Zhang, Z. D. Zhang and X. H. Gao, *CrystEngComm,* 2015, **17**, 3820.
35 J. L. Chen, S. Q. Ma, J. B. Zhang, B. Li, B. Xu and W. J. Tian, *ACS Photonics*, 2015, **2**, 313.
36 Pauling, L. The nature of the chemical bond. 3rd Ed. NY: Cornell Univ*.,* Press, 1960.
37 M. T. Zhang and T. L. Li, *CrystEngComm*, 2014, **16**, 7162.
38 S. Chevreux, C. Allain, L. Wilbraham, K. Nakatani, P. Jacques, I. Ciofini and G. Lemercier, *Faraday Discuss.*, 2015, **DOI:** 10.1039/C5FD00054H.
39 H. W. Kim, J. Jung, M. Han, S. Lim, K. Tamada, M. Hara, M. Kawai, Y. Kim and Y. Kuk, *J. Am. Chem. Soc.*, 2011, **133***,* 9236.
40 (a) H. D. Ju, X. T. Tao, Y. Wan, J. H. Shi, J. X. Yang, Q. Xin, D. C. Zou and M. H. Jiang, *Chem. Phys. Lett*., 2006, **432**, 321; (b) Z. Zheng, Q. Zhang, Z. P. Yu, M. D. Yang, H. P. Zhou, J. Y. Wu and Y. P. Tian, *J. Mater. Chem. C*, 2013, **1**, 822.
41 (a) X. J. Zhang, M. A. Ballem, M. Ahrén, A. Suska, P. Bergman and K. Uvdal, *J. Am. Chem. Soc.*, 2010, **132**, 10391; (b) Y. Sun and B. Yoo, *New J. Chem*., 2015, **39**, 3366.
42 H. J. Lee, W. Cho and M. Oh, *CrystEngComm***,** 2010, **12**, 3959.
43 P. Milosz, A. C. Hazel, G. D. Robert and L. A. Harry, *Angew. Chem., Int. Ed.*, 2009, **48**, 3244.
44 X. Li, Z. Rinkevicius and H. Ågren, *J. Chem. Theory Comput.*, 2014, **10**, 5630.
45 H. P. Zhou, Z. Z, G. Y. Xu , Z. P. Yu, X. F. Yang , L. H. Cheng, *Dyes Pigments,* 2012, 570.
46 (a) L. Y. Zhou, X. B. Zhang, Y. F. Lv, C. Yang, D. Q. Lu, Y. Wu, Z. Chen, Q. L. Liu and W. H. Tan, *Anal. Chem*., 2015, **87**, 5626; (b) S. Biswas, X. H. Wang, A. R. Morales, H. Y. Ahn and K. D. Belfield, *Biomacromolecules*, 2011, **12**, 441.

Graphical abstract for:

Effect of solvent, pH and metal ions on the self-assembly process and optical properties of an A-π-D-π-A type triphenylamine carboxylic acid derivative

Lin Kong, Yun Liu, Hui Wang, Xiao-He Tian, Qi-Yu Chen, Yu-peng Tian, Sheng-li Li, Zhao-ming Xue and Jia-xiang Yang

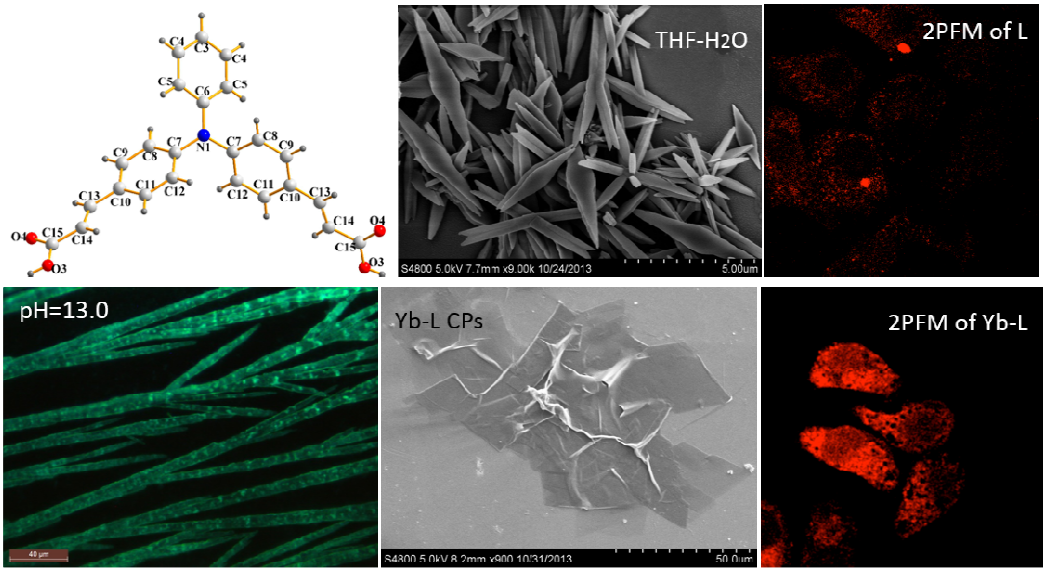

The effect of solvent, pH and metal ion on the morphology and optical properties of a carboxylic-acid derivative was researched.